The Interaction of Flow, Heat Transfer, and Free Interfaces in an Electron-Beam Vaporization System for Metals

K. W. Westerberg
Aspen Technology, Inc.

M. A. McClelland
Lawrence Livermore National Laboratory

B. A. Finlayson
University of Washington

Lawrence Livermore National Laboratory

DISCLAIMER

DISCLAIMER

Portions of this document may be illegible in electronic image products. Images are produced from the best available original document.

THE INTERACTION OF FLOW, HEAT TRANSFER, AND FREE INTERFACES IN AN ELECTRON-BEAM VAPORIZATION SYSTEM FOR METALS

K. W. Westerberg
Aspen Technology, Inc.
Ten Canal Park
Cambridge, MA 02141 U.S.A.

M. A. McClelland*
Lawrence Livermore National Laboratory
P.O. Box 808, L-460
Livermore, CA 94550 U.S.A.

B. A. Finlayson
Department of Chemical Engineering, BF-10
University of Washington
Seattle, WA 98195 U.S.A.

Abstract

A numerical analysis is made of the liquid flow and energy transport in a system to vaporize metals. The energy from an electron beam heats metal confined in a water-cooled crucible. Metal vaporizes from a hot pool of circulating liquid which is surrounded by a shell of its own solid. Flow in the pool is strongly driven by temperature-induced buoyancy and capillary forces and is located in the transition region between laminar and turbulent flow. At high vaporization rates, the thrust of the departing vapor forms a trench at the beam impact site.

A modified finite element method is used to calculate the flow and temperature fields coupled with the interface locations. The mesh is structured with spines that stretch and pivot as the interfaces move. The discretized equations are arranged in an "arrow" matrix and solved using the Newton-Raphson method. The electron-beam power and width are varied for cases involving the high-rate vaporization of aluminum. Attention is focused on the interaction of vaporization, liquid flow, and heat transport in the trench area.

keywords: free surfaces, free convection, electron-beam, finite element method, vaporization

1 Introduction

In recent years, electron-beam technology has become increasingly important in metal processing operations such as physical vapor deposition, welding, refining, casting, and laser isotope separation. These systems can provide a high-performance product with a reduced impact on the environment. An improved understanding of transport processes would yield improvements in throughput, control, and system lifetime.
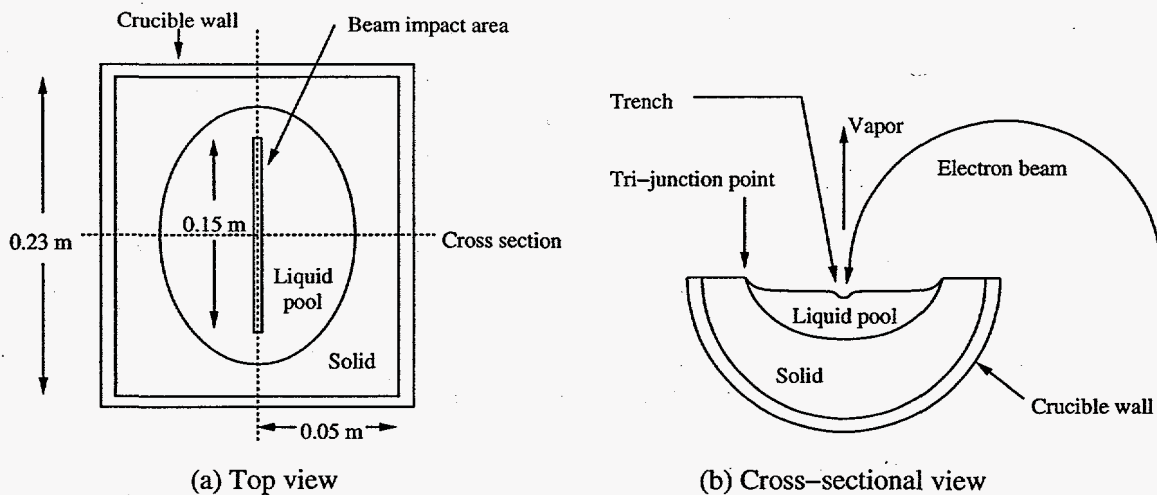
---

*Author to whom correspondence should be addressed.

Figure 1: Experimental electron-beam vaporizer for Aluminum.

In a typical e-beam vaporization system for metals, a melt confined in a water-cooled crucible is heated with the energy from an electron beam (see Figure 1). A small fraction of this energy provides the heat necessary to vaporize the metal. Another portion of the melt energy is lost to thermal radiation and to the formation of "skip" or secondary electrons. The remaining energy is transported by convection and conduction to the cooled crucible wall.

The metal evaporates from a pool of circulating liquid which is surrounded by a solid skull. Flow is driven by thermally-induced gradients in the density (buoyancy effect) and surface tension (Marangoni effect). The flow intensity is high due to the low viscosity of the liquid metal and the large temperature gradients present in the system. At high vaporization rates, a trench forms in the liquid-vapor interface from the thrust of the departing atoms of vapor.

The effects of flow intensity have been examined for buoyancy and capillary-driven flows in shallow rectangular cavities with differentially-heated side walls. In the more careful investigations [1] the critical flow intensity has been determined for which steady-state solutions are unstable to small disturbances. In a recent study by McClelland [2], time-dependent simulations were made at flow intensities as high as those observed in e-beam vaporizer pools. These results were extended to include a deformable free surface and Marangoni effects [3].

Detailed modeling of this system is also a challenge due to the presence of three interfaces joined at a "tri-junction" (see Figure 1b). These interfaces separating solid, liquid, and vapor phases are coupled to the liquid flow and energy transport in the vaporizer. Metal-casting, welding, and crystal-growth systems also share these features.

In an early numerical study of the e-beam vaporizer, Kheshgi and Gresho [4] estimated the locations of the pool boundaries, and calculated the time-dependent flow and temperature fields. Although they benefited from a very efficient computational procedure, the flow and heat transfer problem was decoupled from the interface locations.

A few investigators have analyzed systems with multiple free boundaries joined at a tri-junction. Zacharia, *et al.* [5] developed the method of discrete element analysis on fixed grids to calculate time-dependent flow and temperature fields along with locations for the liquid-gas interface and mushy-zone. In their studies ([5], [6], [7]) of transient, two- and three-dimensional welding systems, they employed upwind differencing often with

coarse grids. Although the intense flows ($Re \sim O(10^2$—$10^4)$) were not fully resolved, favorable comparisons were achieved between calculated and measured surface temperatures and mushy-zone locations.

In studies of the Czochralski crystal growth system, Brown and coworkers ([8], [9]) employed the finite element method with a deforming mesh to track both solid-liquid and liquid- gas interfaces along with the tri-junction. In their method, specified nodes remained at interfaces and the interior nodes moved along spines following the approach described by Kistler and Scriven [10].

Tsai and Kou [11] employed a control volume-finite difference method to analyze flow and heat transfer in a steady-state, two-dimensional welding system. The mesh deformed to track the liquid-gas interface, and a mushy-zone approach was employed for the solid-liquid region. In a study [12] of a floating-zone crystal growth system this approach was extended to provide for the tracking of both the liquid-gas and solid-liquid interface along with a tri-junction. In a later investigation [13] the transport of a second species was included.

In previous studies ([14], [15]) we developed a two-dimensional, steady-state model for the e-beam vaporization of aluminum. Rotating spines were employed in a finite element method to track the horizontal position of the tri-junction and locations of the solid-liquid and liquid-vapor interfaces. The nonlinear equations governing the flow field, temperature field, and free-boundary locations were solved in a coupled manner using a Newton-Raphson method. The electron-beam width and power were varied along with the viscosity and Marangoni contribution. The results show that changes in free boundary locations can weaken the dependence of vapor rate on e-beam power. The calculations also reveal that viscosity decreases can yield relatively small changes in the vaporization rate. The thermal transport improvements from higher circulation rates are approximately canceled by the increased thermal resistance resulting from the formation of flow cells.

In the earlier studies ([14], [15]) the vaporization rates were limited to low values, and a trench local to the e-beam impact area was absent. In this investigation, these limitations are removed with improvements in the material-inventory constraints. Results are given for the high-rate vaporization of aluminum in which the electron-beam power and width are varied.

2 Model Equations

We consider the steady-state flow and heat transport in a symmetry plane of the e-beam vaporization system shown in Figure 1. The assumption of a two-dimensional system is valid to the extent that field curvature effects can be neglected in the out-of-plane direction. The domain is further reduced to the right-half plane by assuming that the flow and temperature fields are symmetric about a center line. Field equations for flow and heat transport are included in the liquid and solid phases, but the effects of the vapor phase are incorporated through the use of boundary conditions at the top surface of the melt.

2.1 Field Equations

Flow in the pool is governed by the steady-state continuity and momentum equations for a Newtonian liquid:

$$\nabla \cdot \underline{u} = 0 \tag{1}$$

$$\rho \underline{u} \cdot \nabla \underline{u} = -\nabla p + \mu \nabla^2 \underline{u} + \rho \underline{g}[1 - \beta(T - T_0)] \tag{2}$$

In the absence of compressive work and viscous dissipation, the energy equation takes the form

$$\rho C_p \underline{u} \cdot \nabla T = k \nabla^2 T \tag{3}$$

3

In the solid phase, there is no flow, and the left-hand-side of Eqn. (3) vanishes.

Following the Boussinesq approximation, the liquid density varies linearly with temperature about a reference value, ρ_0, evaluated at the melting-point temperature. All other physical properties in Eqns. (1)-(3) are taken to be constant within a given phase.

The Reynolds and Peclet numbers provide measures of the flow intensity and thermal convection, respectively:

$$Re = \frac{\rho u_{max} d_{pool}}{\mu} \qquad Pe = \frac{u_{max} d_{pool}}{\alpha}$$

The characteristic length in the above expression is the depth of the liquid pool at the symmetry line, d_{pool}. The maximum surface speed, u_{max}, is the characteristic velocity.

2.2 Material constraints and boundary conditions

2.2.1 Mass inventory and phase distribution

Two constraints are applied for the inventory of solid and liquid material in the crucible. The first condition is a specification for the average level of material in the crucible, $\bar{h}_0$:

$$\bar{h}_{ls} \equiv \frac{\int_0^{x_w} h\, dx}{x_w} = \bar{h}_0 \tag{4}$$

Here x_w is the x-coordinate of the junction where the crucible wall, solid metal, and vapor meet (endpoint 10 in Figure 2). The second condition is that the solid-vapor interface has a uniform elevation:

$$h = h_s \quad \text{for} \quad x_{tri} \leq x \leq x_w \tag{5}$$

With the assumption of uniform material density, these two conditions determine the amount of mass in the crucible. The combination of Eqns. (4) and (5) yields a relationship for the average level of liquid in the pool:

$$\bar{h}_l = \frac{\bar{h}_{ls} x_w - h_s(x_w - x_{tri})}{x_{tri}} \tag{6}$$

As an alternative, $\bar{h}_l$ and h_s could be specified, and $\bar{h}_{ls}$ would be a function of these two elevations (see Eqn. (6)).

There are limits to the supportable difference between the liquid and tri-junction levels. For metal systems, the variations in surface hydrostatic pressure that accompany changes in liquid level are primarily balanced by surface tension forces. This balance can be established when the level change has the scale of the capillary length, $L_c = (\sigma/\rho g)^{1/2}$, in which σ is the surface tension. Significantly larger variations in the surface elevation cannot be supported by surface tension and numerical solutions will not be available. In practice, the melt system would relocate the tri-junction at a different elevation. For example, liquid from a pool of high elevation would overflow on to the solid-vapor interface and solidfy, raising the level of this interface and tri-junction.

In earlier papers ([14], [15]) the mass inventory constraint (Eqn. (4)) was not used, resulting in a "natural" pool level which was determined by the mechanics of flow. The addition of Eqn. (4) provides a much better model, since the pool level can be varied as it is in practice. A comparison of results for these two approaches is given in section 4.
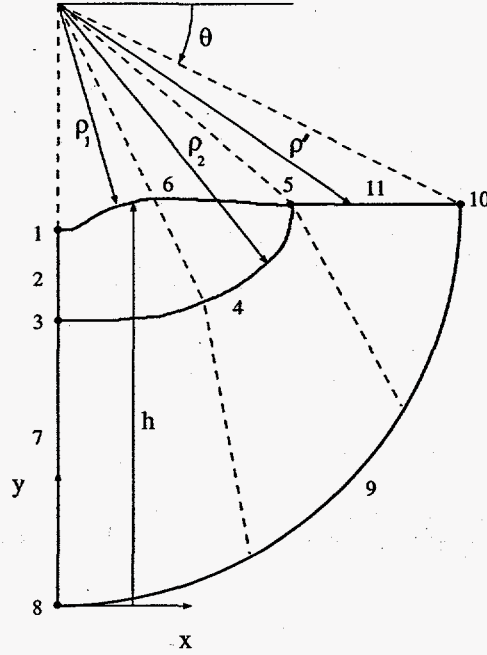
Figure 2: Mesh variables, spines (- - -) and interfacial segments and endpoints. The interfacial variables and associated conditions are given in Table 1.

2.2.2 Flow boundary conditions

For the specification of flow conditions at the pool boundaries, it is assumed that the vaporization rate is sufficiently small that vaporization and makeup feed have a negligible kinematic effect on the flow field. All pool boundaries are then material boundaries, and the interfacial flow obeys the steady-state kinematic equation:

$$\underline{n} \cdot \underline{u} = 0 \tag{7}$$

At the symmetry line the shear stress vanishes, and the tangential velocity is zero at the solid-liquid interface:

$$\underline{n} \cdot \underline{\underline{\tau}} \cdot \underline{t} = 0 \quad \text{at} \quad x = 0 \tag{8}$$

$$\underline{t} \cdot \underline{u} = 0 \tag{9}$$

A force balance at the liquid-vapor interface gives

$$\underline{M} \equiv \underline{n} \cdot \left(p\underline{\underline{\delta}} + \underline{\underline{\tau}} \right) + \sigma \frac{d\underline{t}}{ds} - \underline{n}\pi_v = 0 \tag{10}$$

The second term in Eqn. (10) is the normal force resulting from deformation of the interface. The surface tension, σ, is taken to be constant at its melting-point value. Marangoni effects, induced by variations in the interfacial temperature, are not included in this study. The third term in Eqn. (10) is the normal force generated by the thrust of the departing vapor. For the vaporization of ideal atoms at low rates, the vapor thrust is approximated by [16]:

$$\pi_v = \frac{p_{vap}(T)}{2} \tag{11}$$

5

Table 1: Interfacial conditions and variables for the segments and endpoints shown in Figure 2.

segment or endpoint	$\underline{u}$	p	T	θ	ρ_1	ρ_2	ρ'
1	u_x, M_y	c	q_{lv}, q_0	f	u_y	–	–
2	u_x, τ_{yx}	c	q_0	–	–	–	–
3	u_x, u_y	$\overline{h}_{ls}$	q_{sl}, q_0	–	–	T_{mp}	–
4	u_x, u_y	c	q_{sl}	–	–	T_{mp}	–
5	u_x, u_y	c	q_{sl}, q_{lv}	T_{mp}	–	–	h_s
6	$\underline{M}$	c	q_{lv}	θ_{tri}	u_n	–	–
7	–	–	q_0	–	–	–	–
8	–	–	q_0, q_w	–	–	–	–
9	–	–	q_w	–	–	–	–
10	–	–	q_w, q_0	f	–	–	f
11	–	–	q_0	θ_{tri}	–	–	h_s

c	–	continuity, Eqn. (1)	q_w	–	wall thermal, Eqn. (21)
f	–	fixed variable	q_0	–	insulated boundary, Eqn. (20)
$\overline{h}_{ls}$	–	material level, Eqn. (4)	T_{mp}	–	isotherm, Eqn. (18)
h_s	–	solid level, Eqn. (5)	u_n	–	kinematic, Eqn. (7)
$\underline{M}$	–	liq-vap momentum, Eqn. (10)	u_x	–	$u_x = 0$
M_y	–	surface normal cond., Eqn. (23)	u_y	–	$u_y = 0$
q_{lv}	–	liq-vap thermal, Eqn. (13)	θ_{tri}	–	Eqn. (22)
q_{sl}	–	sol-liq thermal, Eqn. (19)	τ_{yx}	–	$\tau_{yx} = 0$, Eqn. (8)

Since Eqn. (10) includes surface tension, two endpoint conditions are required. At the symmetry line, the interface is horizontal:

$$\underline{n} = \underline{\delta}_y \quad \text{at} \quad x = 0 \tag{12}$$

The other endpoint is a tri-junction where vapor, liquid, and solid phases meet. We take this junction to be located at a sharp edge with specified elevation h_s (see Eqn. (5)). An improved description would incorporate the specification of a contact angle rather than the elevation.

2.2.3 Thermal boundary conditions

At the liquid-vapor interface an energy balance accounts for the power provided by the electron beam and the energy losses due to vaporization and thermal radiation:

$$\underline{n} \cdot \underline{q} = (-\underline{n} \cdot \underline{\delta}_y)q_b + q_v + q_r \tag{13}$$

The energy flux from the electron beam is assumed to follow a Gaussian distribution:

$$q_b = \frac{\gamma Q_b}{\sqrt{2\pi}\sigma_b L_b} e^{-x^2/2\sigma_b^2} \tag{14}$$

Some of the incident energy is lost to the formation of skip electrons, and the coefficient γ is the fraction of incident energy absorbed by the melt pool. The vaporization energy loss

includes kinetic energy and latent heat contributions:

$$q_v = n_v \left(\frac{2RT}{M} + \Delta H_{vap} \right) \tag{15}$$

For low vaporization rates, the vapor mass flux, n_v, is approximated by

$$n_v = p_{vap}(T) \left(\frac{M}{2\pi RT} \right)^{1/2} \tag{16}$$

The heat flux resulting from radiant heat exchange with the surroundings is

$$q_r = \varepsilon(T)\sigma_{SB}(T^4 - T_\infty^4) \tag{17}$$

in which T_∞ represents the temperature of the surroundings.

For steady-state conditions, the temperature at the solid-liquid interface is the melting-point value:

$$T = T_{mp} \quad \text{at} \quad \underline{x} = \underline{x}_{sl} \tag{18}$$

An energy balance at the solid-liquid interface yields

$$\underline{n} \cdot (k\nabla T)|_l = \underline{n} \cdot (k\nabla T)|_s \tag{19}$$

and there is no flow of energy across the symmetry line:

$$\underline{n} \cdot \underline{q} = 0 \quad \text{at} \quad x = 0 \tag{20}$$

Newton's law of cooling is used to describe the transfer of energy between the solid metal and the crucible cooling water with temperature T_w.

$$\underline{n} \cdot \underline{q} = h_w(T - T_w) \tag{21}$$

The heat transfer coefficient, h_w, is taken to be uniform, and it includes the resistance due to metal-metal contact, solid conduction in the crucible wall, resistance due to metal-water contact and energy transport in the water.

3 Finite Element Method

3.1 Mesh Parameterization

Deforming meshes structured with spines [10] are used to track the liquid-vapor and solid-liquid interfaces (see Figure 2). Specified nodes remain on interfaces while interior nodes move along these spines. In order to treat the solid-liquid interface which moves horizontally at the tri-junction and vertically at the symmetry plane, we employ spines that emanate from a single "anchor" point above the liquid-vapor interface on the symmetry line. Each spine intersects the top surface of the vaporizer and bends at the solid-liquid or liquid-vapor interface before continuing to base points distributed along the crucible wall.

For each spine passing through the liquid, there are three variables (see Figure 2). The coordinates ρ_1 and ρ_2 are the respective distances from the anchor point to the liquid-vapor and liquid-solid interfaces. There is also a pivot angle, θ, to accommodate the horizontal motion of the tri-junction. For a spine passing only through the solid, a single coordinate ρ' is used along with the pivot angle. A spine is completely parameterized with these three coordinates along with the anchor and base point locations.

We use several relationships to insure the smooth deformation of the mesh. First, the relative spacing of nodes is preserved along a spine within each material phase. Second, the angular deformation of the mesh is oriented about the motion of the tri-junction:

$$f(\theta_i, \theta_{tri}) = 0 \tag{22}$$

7

3.2 Discretization

The field equations (1)-(3) and boundary conditions are discretized using the Galerkin finite element method [17], [18]. The velocities, temperatures, and coordinate mapping are represented by two-dimensional quadratic basis functions, and the pressure is represented by linear basis functions. The weak forms of the momentum and energy equations are used in which the interfacial stress and heat flux conditions are incorporated as natural boundary conditions.

The discretized versions of the field equations (1)-(3) are applied at interior locations in the usual manner, but the treatment of boundary conditions is more complex. In Table 1, boundary conditions and associated variables are listed for the interfacial segments and endpoints shown in Figure 2. (Note that segments do not include endpoints.) Special attention is given to conditions at endpoints and "distinguished" conditions which are associated with the determination of free boundary variables.

At the center-line node on the top surface (endpoint no. 1) the flow is stagnant ($\underline{u} = 0$), and the symmetry condition Eqn. (12) for the liquid-vapor interface is applied in its natural form [10]:

$$\underline{n} \cdot \underline{M} = 0 \quad \text{at} \quad x = 0 \tag{23}$$

Here $\underline{M}$ is the force balance Eqn. (10) at the liquid-vapor interface. This condition is distinguished since it is applied for the determination of ρ_1. For convenience in assembling the solution matrices, Eqn. (23) and the condition $u_y = 0$ are switched with respect to their associated variables.

At the center-line point on the solid-liquid interface (endpoint no. 3) the continuity equation is replaced by the liquid level condition Eqn. (4). In effect, the liquid pressure at this location is adjusted so that a specified level of material is maintained in the melt.

It is noted that the liquid level condition (Eqn. (4)) at endpoint no. 3, could not be employed with the flow conditions at endpoint no. 1 in the earlier studies ([14], [15]). In these previous studies, Eqn. (10), was employed at endpoint no. 1 with the condition $\underline{t} = \underline{\delta}_x$. In addition, the kinematic condition (Eqn. (7)) was applied as the distinguished condition. This formulation was not used in this study since the loss of a continuity equation (endpoint no. 3) combined with $\underline{u} \neq 0$ and high liquid pressures at endpoint no. 1 resulted in significant material leakage across the symmetry line.

At the solid-liquid interface (segment no. 4) and tri-junction (endpoint no. 5) the melting-point specification, Eqn. (18) is applied as the distinguished condition for the variables ρ_2 and the angular position θ, respectively. At the liquid-vapor interface, the kinematic condition (Eqn. (7)) is the constraint associated with the variable ρ_1. All other conditions involve the distribution of elements or the conventional application of essential and natural boundary conditions.

3.3 Solution of Residual Equations

The Newton-Raphson method is used to solve the nonlinear algebraic equations for the velocity, pressure, and temperature fields along with the interface locations. In the formulation of the matrix problem, the field equations and surface equations are differentiated with respect to field and interface variables. The resulting expressions are arranged as an "arrow" matrix with a "shaft" of banded field equations and an "arrow head" incorporating interface contributions. An efficient solution procedure for this partially-banded matrix problem is described by Westerberg, *et al.* [19]. The assembly and elimination of the field equations is performed using the frontal method [20].

8

4 Results

Steady-state calculations were performed for the vaporization of pure aluminum. The majority of the physical properties are evaluated at the melting temperature of 660 °C and are taken to be uniform within a given material phase (see Table 2). However, the temperature-dependence is included in the emissivity $\varepsilon(T)$ and the vapor pressure $p_{vap}(T)$. As discussed in detail below, the viscosity is a factor of five larger than the physical value.

Table 2: Material properties of aluminum.

ρ	=	2370 kg/m^3	$p_{vap}(T)$	=	$p_1 \exp(E/RT)$
β	=	1.11×10^{-4} °C^{-1}	p_1	=	8.25×10^{10} N/m^2
k	=	94 W/m-K	E	=	-3.10×10^5 J/mole
k_s	=	197 W/m-K	R	=	8.314 J/mole-K
μ_{meas}	=	0.00125 kg/m-s	$\varepsilon(T)$	=	$a_1(rT)^{1/2} - a_2 rT$
$\mu^\star = \mu/\mu_{meas}$	=	5	a_1	=	5.76 (ohm-m-K)$^{-1/2}$
α	=	3.36×10^{-5} m/s^2	a_2	=	12.4 (ohm-m-K)$^{-1}$
σ	=	0.865 N/m	r	=	2.35×10^{-7} ohm-m
ΔH_{vap}	=	1.15×10^7 J/kg	γ	=	0.83

Table 3: Parameters for aluminum inventory, electron-beam configuration, and crucible cooling.

Q_b	=	50 — 80 (70) kW	$T_w = T_\infty$	=	25 °C
σ_b	=	1.5 — 6.0 (3.0) $\times 10^{-3}$ m	$\bar{h}_0$	=	4.95×10^{-2} m
L_b	=	0.15 m	h_s	=	5.00×10^{-2} m
h_w	=	10,000 W/m^2-K	x_w	=	0.05 m

Operating parameters for the vaporization system shown in Figure 1 are listed in Table 3. The average level of material in the crucible ($\bar{h}_0 = 4.95 \times 10^{-2}$ [m]) is taken to be slightly lower than the solid level ($h_s = 5 \times 10^{-2}$ [m]) as would generally be seen in practice. A range of values is considered for the electron-gun power and the width of the e-beam. The heat-transfer coefficient is chosen to be 10,000 [W/m^2-K] which indicates good contact between the aluminum and the crucible. This value is somewhat higher than values given in a recent compilation of metal-mold interfacial coefficients [21].

In this study, results were first obtained for a "base case". (Base case values are denoted by "()" when a range of values is given in Table 3). As mentioned above the base-case viscosity is a factor of five greater than the physical value. At lower values for the viscosity, the flow is more intense and difficult to resolve. The search for steady-state solutions is more difficult, making a parameter study less tractable.

In an earlier study [15] of this same vaporization system at different conditions, the viscosity ratio $\mu^\star = \mu/\mu_{meas}$ was varied from 1.25 to 20. As $\mu^\star$ decreased from 5 to 1.25 the vaporization rate increased by a relatively small 13% even though the details of the flow field changed significantly. Changes in the thermal transport characteristics were relatively small as increases associated with higher flow velocities were offset by the formation of additional flow cells. Thus, results for the base case ($\mu^\star = 5$) should provide relevant physical insight despite the artificially high viscosity.

$$\rightarrow\!\mid 2\sigma_b \mid\!\leftarrow$$

(a)　　　　(b)

(c)

T [C]			
a	1600	e	800
b	1400	f*	660
c	1200	g	600
d	1000	h	400
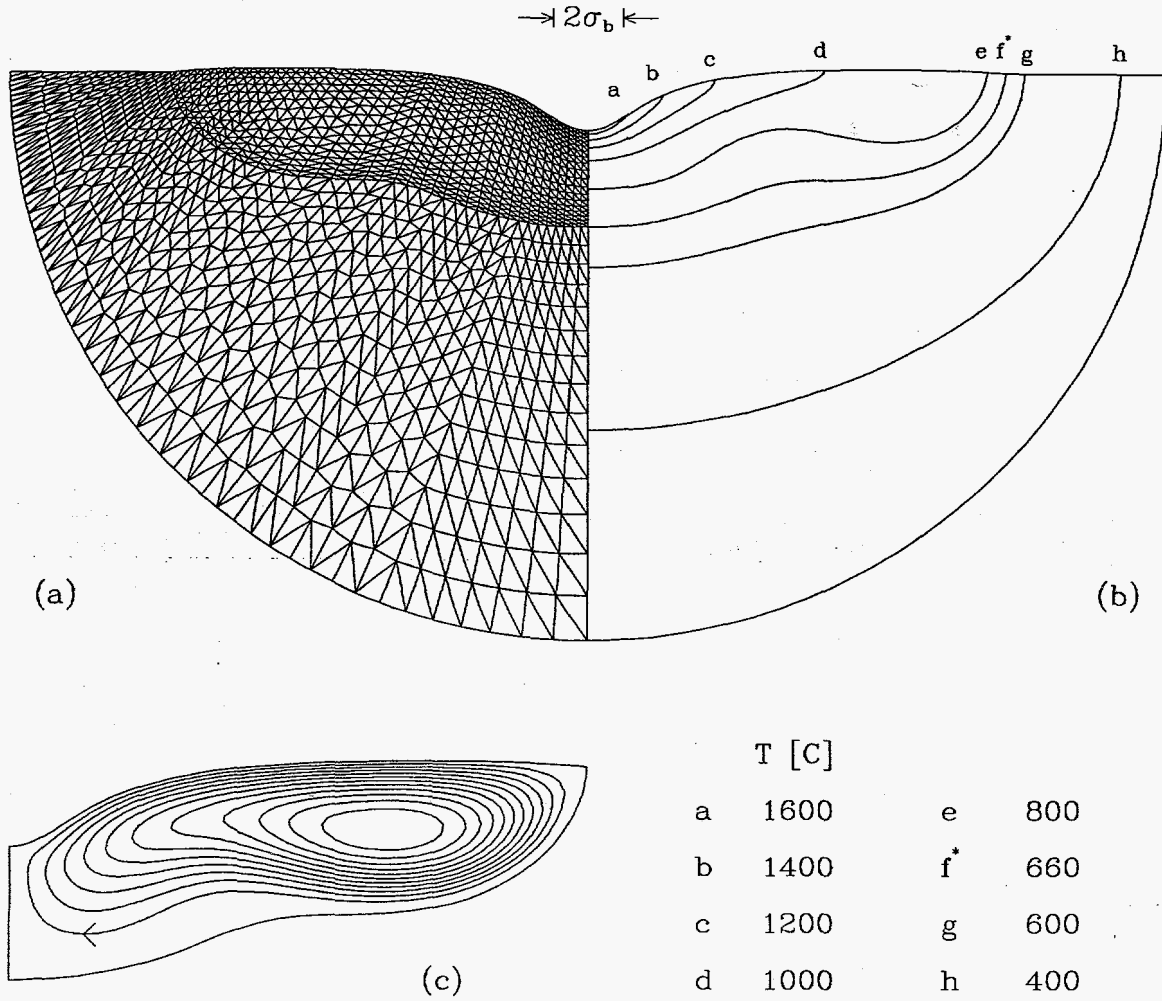
Figure 3: Results for base case (material properties and operating parameters listed in Tables 2 and 3) on mesh M2. (a) Deformed mesh, (b) Temperature contours, (c) Stream-function contours.

4.1　Base case

Calculations were made on a coarse mesh M1 with 5027 unknowns and a fine mesh M2 with 11,105 unknowns. A deformed fine mesh for the base case is shown in Figure 3a. The elements are concentrated near the pool boundaries where the gradients are largest. The spines originate from an anchor point 0.03 [m] above the solid-vapor interface along the center line ($x = 0$).

There is a significant trench in the vicinity of the beam impact area resulting from the thrust of the departing vapor (see Figure 3). The trench is of sufficient volume to force liquid above the level of the solid-vapor interface as a consequence of the mass inventory expression, Eqn. (4). With reference to this level, the depth of the trench is 5.11 [mm] which is comparable to the capillary length of L_c=6.10 [mm]. The widths of the trench and beam are of the same scale.

In the right half of the pool, the liquid circulates in a clockwise direction within a single cell. The horizontal convection of energy away from the beam impact area "drives" the tri-junction towards the crucible wall, creating a shallow pool with aspect ratio w_{pool}/d_{pool}=8.46. The flow is of moderate intensity (Re=276), and inflections are visible in the streamlines

near the solid-liquid interfaces. With further decreases in viscosity, these inflections would become more pronounced and a second cell would form ([15], [1]). Another contribution to these inflections is the trench which drives the thermal field and pool downwards near the center line. Note that the solid-liquid interface follows the contour of the nearby streamlines as a result of moderate thermal convection (Pe=21.7).

The energy balance of Table 4 shows that only 6.2% of the energy is used for vaporization. Large fractions are lost to the crucible and the formation of secondary electrons whereas a small percentage is lost to thermal radiation. The energy flow balances to 1.1% and 0.3% for the M1 and M2 meshes, respectively.

Table 4: Heat-losses as a percentage of incident e-beam power (70 [kW]) for base case.

Contribution	Mesh M1	Mesh M2
crucible	77.4	76.6
secondary electrons	17.0	17.0
vaporization	6.2	6.2
thermal radiation	0.5	0.5
total	101.1	100.3

The aluminum vaporization rate for the base case is 1.24 [kg/h] (3.44×10^{-4} [kg/s]). This value is in the general range of 0.1—50 [kg/h] (3×10^{-5} — 1×10^{-2} [kg/s]) for commercial systems which have e-beam power capacities ranging from 10—250 [kW] ([22], [23]). In the earlier studies ([14], [15]) a small maximum vapor rate of 2.43×10^{-2} [kg/h] (6.76×10^{-6} [kg/s]) was achieved at 30 [kW]. Without the material level constraint (Eqn. (4)), the average pool level decreased with e-beam power without forming a local trench. The application of Eqn. (4) maintains the pool level, providing the hydrostatic forces to balance the thrust of the departing vapor. The local trench is formed as liquid is displaced from the beam impact area to other regions of the pool.
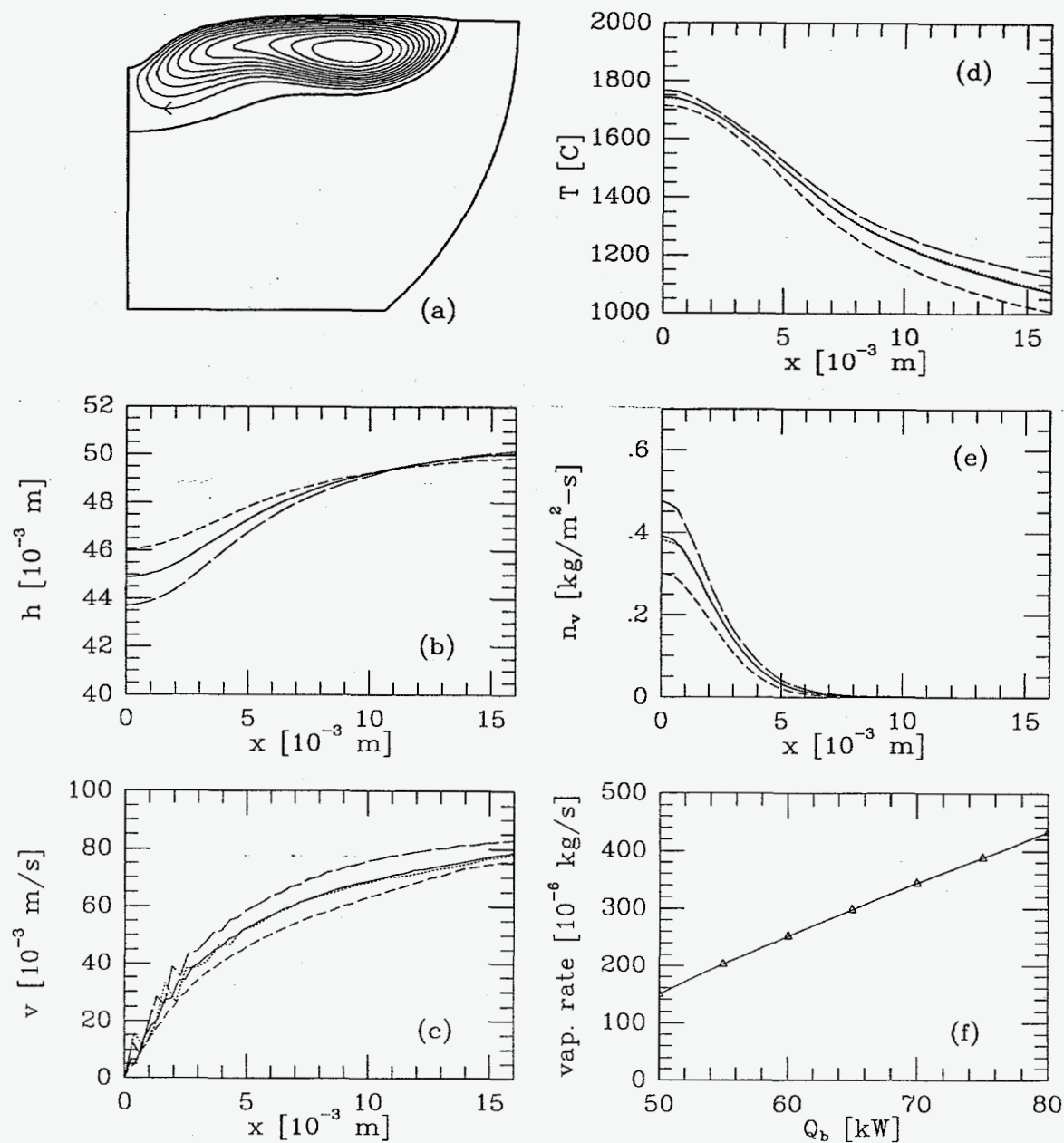
4.2 E-beam power variations

Calculations were performed in which the e-beam power Q_b was varied from 50 to 80 [kW] and all other parameters and properties had their base-case values (see Figure 4). It is noted that numerical convergence was not achieved at a gun power of 85 [kW] for either mesh. For Q_b=80 [kW], the stream function and pool boundary are plotted in Figure 4a. For Q_b=60, 70, and 80 [kW] the surface level, speed, temperature, and vaporization flux are plotted versus x in the trench area (see Figures 4b-e). Finally, the vaporization rate is plotted versus beam power in Figure 4f.

The streamlines are smooth, suggesting that the flow field is well resolved (see Figure 4a). However, the surface velocity profiles of Figure 4c show spurious oscillations near the center line which increase with beam power. For Q_b=70 [kW] differences in the curves for the two meshes are noticeable. The growth of these oscillations may have contributed to the lack of numerical convergence at Q_b=85 [kW] that was mentioned above. However, all of the pool boundaries along with temperature, and vaporization profiles are well resolved. Differences between these results for the two meshes are generally very small (see Figure 4b, d, e, and f). Since these are often the key variables of interest, the marginal resolution for the flow field can be tolerated.

As the power is increased from 70 to 80 [kW], the width of the pool increases by 12.0 [mm], but the center-line depth decreases by 0.27 [mm] (see Figures 3c and 4a). The

Figure 4: Effects of variations in e-beam power. (a) Stream-function contours for Q_b=80 [kW]. Surface variables in trench area: (b) elevation, (c) velocity, (d) temperature, (e) vapor flux for Q_b=60 [kW] and M2 mesh (-----), Q_b=70 [kW] and M2 mesh (———), Q_b=80 [kW] and M2 mesh (———), and Q_b=70 [kW] and M1 mesh (··········). (f) Vaporization rate versus beam power for M1 and M2 meshes (curves coincide to resolution of plot).

additional 10 [kW] is primarily transported towards the crucible wall near the solid-vapor interface.

For $60 \leq Q_b \leq 80$ [kW], the trench width is of the same scale as the beam width (see Figure 4b). Also, the trench depth increases approximately linearly with gun power which is a significant result given the strong dependence of vapor pressure and thrust on temperature (see Eqn. (11) and Table 2). The vapor pressure doubles for a temperature increase of 76 [°C] at 1750 [°C]. This vaporization system with free boundaries has a significant capacity to relieve thermal and mechanical stress. The surface temperature at the center line increases only 51 [°C] for a 33% increase in power (see Figure 4d). This increase compares with 110 [°C] at a location x=0.016 [m] outside the trench area.

There are a number of effects that accompany the gun power increases. As the trench deepens, its area increases, reducing the energy flux. In addition, the trench is closer to the cold crucible wall, decreasing the resistance to energy transport. Also, increases in the vaporization energy losses are concentrated in the trench area (see Figure 4e and Table 4). Finally, increases in the circulation rate accelerate the rate at which energy is transported away from the trench area (see Figure 4c).

For $50 \leq Q_b \leq 80$ [kW], the dependence of the vaporization flux and rate on power is also nearly linear (see Figures 4e and f). At lower powers (not shown), the trench is shallower and the curvature of the vapor rate-power profile is larger. The curves for the vapor flux show that most of the metal is vaporized from the trench area (see Figure 4e).

4.3 Beam-width variations

Calculations were performed in which the beam width σ_b was varied from 1.5 to 6.0 [mm] with all other parameters having the base-case values (see Figure 5). Calculations converged using the coarse M1 mesh for $2.5 \leq \sigma_b \leq 6$ [mm] and the fine M2 mesh for $1.5 \leq \sigma_b \leq 3$ [mm]. The narrower range of convergence for the fine mesh was characteristic of the calculations of this study.
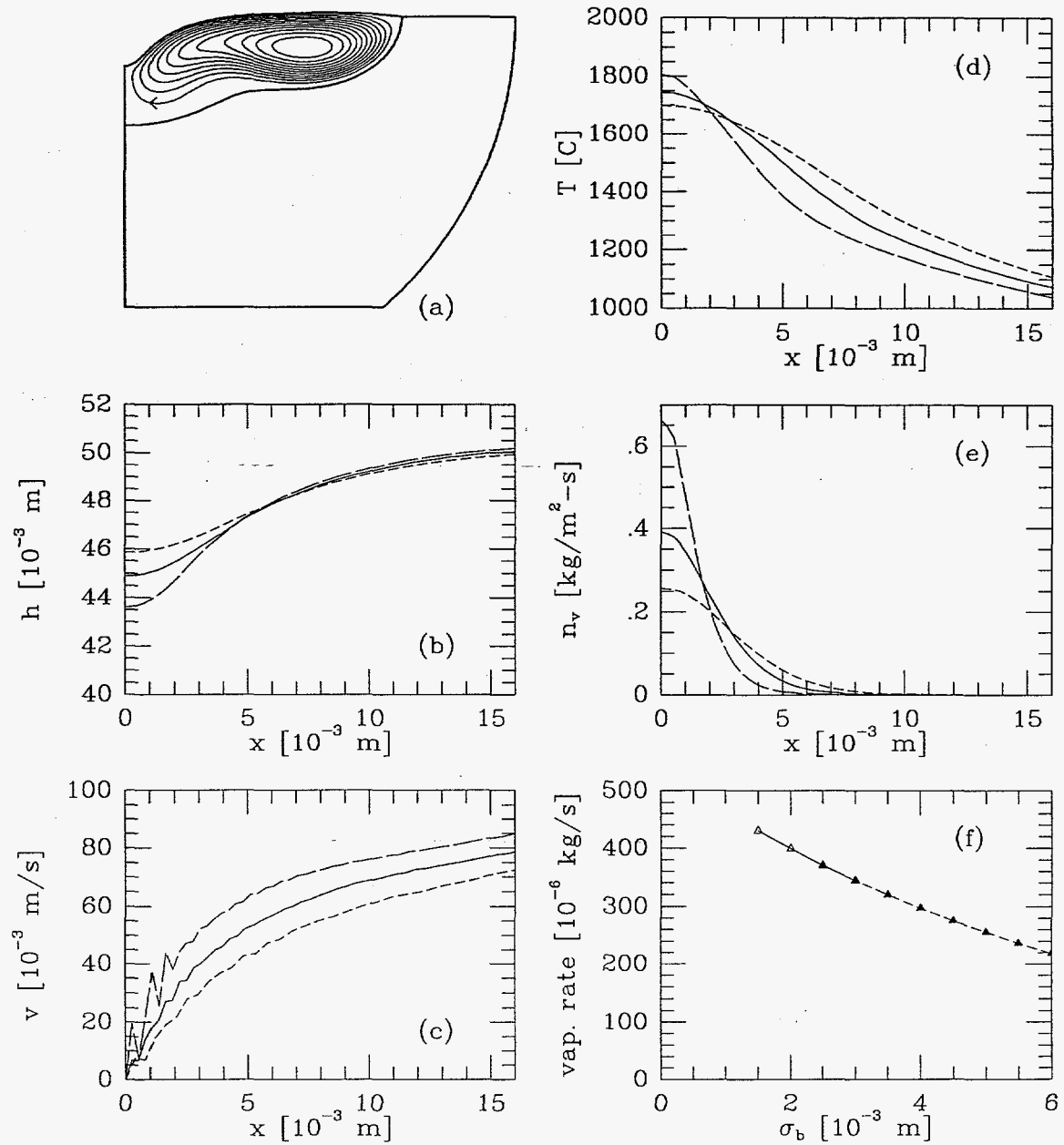
Stream function contours are shown in Figure 5a for a beam width of 2 [mm]. Profiles for the surface height, velocity, temperature, and vaporization flux are plotted in Figures 5b-e for beam width values of 2, 3, and 4 [mm]. Finally, the vaporization rate is plotted versus beam width in Figure 5f, and results from both meshes are included to span the beam-width range.

At $\sigma_b = 2$ [mm], the stream function contours are smooth, but the surface velocity profiles exhibit some spurious fluctuations which decrease with beam width (see Figures 5a and 5c). The pool boundaries, temperature profiles, and vaporization curves are all well resolved.

As σ_b decreases from 3 to 2 [mm], the trench deepens, but there is little change in the position of the solid-liquid interface (see Figures 3b and 5a). At the center line, the variation of trench depth with beam width is slightly stronger than linear. As σ_b decreases, the surface temperature and vapor flux increase near the center line, but decrease in the region outside the trench area (see Figures 5d and 5e).

For a four-fold change in beam width, the vaporization rate nearly doubles from 2.18×10^{-4} to 4.30×10^{-4} [kg/s] (see Figure 5f). Similar to the trench depth, the dependence of vaporization rate on σ_b is slightly stronger than linear. As was the case for the beam-power variations, this vaporization system with free boundaries reduces the concentration of e-beam power that would otherwise lead to much larger increases in the vaporization rate.

Figure 5: Effects of variations in the Gaussian beam width, σ_b. (a) Stream-function contours for $\sigma_b=2$ [mm]. Surface variables in trench area: (b) elevation, (c) velocity, (d) temperature, (e) vapor flux for $\sigma_b=4$ [mm] and M2 mesh (-----), $\sigma_b=3$ [mm] and M2 mesh (———), and $\sigma_b=2$ [mm] and M2 mesh (———). (f) Vaporization rate versus e-beam width for M1 (▲--▲--▲) and M2 (△——△——△) meshes.

14

5 Conclusions

A steady-state model is developed for an e-beam vaporization system which includes the interaction of interfaces with material and energy flow. Solutions are obtained with a modified Galerkin finite element method in which meshes structured with pivoting spines deform to track the location of solid-liquid and liquid-vapor interfaces joined at a tri-junction. The discretized equations are arranged in an arrow matrix and solved with the Newton-Raphson method for the flow and temperature fields along with the interface locations.

Simulations were performed for an aluminum vaporization system in which the electron-beam power and width were varied. The dependence of the vapor rate on these two variables is approximately linear despite the strong effect of temperature on the surface vaporization flux. As the trench deepens, increases in the surface temperature and vaporization flux are reduced by two primary effects. The path for heat transport to the crucible wall is decreased and the e-beam energy flux is reduced by the increased trench area. From these results, it is clear that at high vaporization rates, an accurate model needs to include the deformation of free boundaries coupled with material and energy flow.

Acknowledgement

Nomenclature

C_p	heat capacity	$\underline{t}$	unit tangent vector	
d_{pool}	melt pool depth at $x=0$	T	temperature	
$\underline{g}$	gravitational acceleration vector	T_{mp}	melting point	
		$\underline{u}$	fluid velocity vector	
h	local interface elevation	u_{max}	maximum fluid velocity	
$\overline{h}_0$	average elevation of metal in crucible	x, y	cartesian coordinates	
		α	thermal diffusivity	
$\overline{h}_l$	average elevation of metal in pool	β	vol. expansion coefficient	
		γ	skip coefficient	
h_s	elevation of solid	$\underline{\underline{\delta}}$	unit tensor	
h_w	wall heat-transfer coeff.	$\underline{\delta}_x, \underline{\delta}_y$	unit vector in coordinate direction	
ΔH_{vap}	heat of vaporization			
k	thermal conductivity	ε	emissivity	
L_b	electron-beam length	μ	viscosity	
L_c	capillary length	π_v	vapor thrust	
M	molecular weight	ρ	density	
$\underline{M}$	surface force balance	$\rho_1, \theta, \rho_2, \rho'$	spine variables	
$\underline{n}$	unit normal vector	σ	surface tension	
n_v	evaporative mass flux	σ_b	gaussian beam width	
p	pressure	σ_{SB}	Stefan-Boltzman constant	
Pe	Peclet number	$\underline{\underline{\tau}}$	stress tensor	
p_{vap}	vapor pressure	**subscripts**		
$\underline{q}$	heat flux vector	0	reference state	
q_b	electron-beam heat flux	l	liquid phase	
q_r	radiative heat flux	lv	liquid-vapor interface	
q_v	evaporative heat flux	s	solid phase	
Q_b	electron-beam power	sl	solid-liquid interface	
R	gas constant	tri	tri-junction	
Re	Reynolds number	w	crucible wall	
s	arc-length coordinate	∞	surroundings	

References

[1] B. Roux, G. de Vahl Davis, M. Deville, R. L. Sani, and K. H. Winters. General synthesis of the results. In B. Roux, editor, *Numerical simulation of oscillatory convection in low-Pr fluids*, pages 285–304. Vieweg, 1990.

[2] M. A. McClelland. Application of streamwise diffusion to time-dependent free convection of liquid metals. *Int. J. Numer. Methods Fluids*, vol. 19, pp. 1061–1071, 1994.

[3] M. A. McClelland. Time-dependent liquid metal flows with free convection and a deformable free surface. *Int. J. Numer. Methods Fluids, in press*, 1995.

[4] H. S. Kheshgi and P. M. Gresho. Analysis of electron-beam vaporization of refractory metals. In R. Bakish, editor, *Electron Beam Melting and Refining State of the Art 1986*, pages 68–79. Bakish Materials Corp., Englewood, NJ, 1986.

[5] T. Zacharia, A. H. Eraslan, D. K. Aidun, , and S. A. David. Three-dimensional transient model for arc welding process. *Metall. Trans. B*, vol. 20B, pp. 645–659, 1989.

[6] T. Zacharia, S. A. David, J. M. Vitek, and H. G. Kraus. Computational modeling of stationary gas-tungsten-arc weld pools and comparison to stainless steel 304 experimental results. *Metall. Trans. B*, vol. 22B, pp. 243–257, 1991.

[7] T. Zacharia, S. A. David, and J. M. Vitek. Understanding heat and fluid flow in linear GTA welds. In S. A. David and J. M. Vitek, editors, *International Trends in Welding Science and Technology*, volume 3, pages 27–31. ASM International, Ohio, 1992.

[8] P. A. Sackinger, R. A. Brown, and J. J. Derby. A finite element method for the analysis of fluid flow, heat transfer and free interfaces in Czochralski crystal growth. *Int. J. Numer. Methods Fluids*, vol. 9, pp. 453–492, 1989.

[9] R. A. Brown, T. A. Kinney, P. A. Sackinger, and D. E. Bornside. Toward an integrated analysis of czochralski growth. *J. Crystal Growth*, vol. 97, pp. 99–115, 1989.

[10] S. F. Kistler and L. E. Scriven. Coating flows. In J. R. A. Pearson and S. M. Richardson, editors, *Computational analysis of polymer processing*, pages 243–299. Applied science publishers, London, 1983.

[11] M. C. Tsai and S. Kou. Marangoni convection in weld pools with a free surface. *Int. J. Numer. Methods Fluids*, vol. 9, pp. 1503–1516, 1989.

[12] G. W. Lan and S. Kou. Heat transfer, fluid flow and interface shapes in floating-zone crystal growth. *J. Crystal Growth*, vol. 108, pp. 351–366, 1991.

[13] G. W. Lan and S. Kou. Radial dopant segregation in zero-gravity floating-zone crystal growth. *J. Crystal Growth*, vol. 132, pp. 578–591, 1993.

[14] K. W. Westerberg, M. A. McClelland, and B. A. Finlayson. The tracking of interfaces in an electron-beam vaporizer. In R. W. Lewis, editor, *Numerical Methods in Thermal Problems*, volume VIII, Pt. 2, pages 1322–1333. Pineridge Press, Swansea, 1993.

[15] K. W. Westerberg, M. A. McClelland, and B. A. Finlayson. Numerical simulation of material and energy flow in an e-beam melt furnace. In R. Bakish, editor, *Electron Beam Melting and Refining State of the Art 1993*, pages 153–165. Bakish Materials Corp., Englewood, NJ, 1993.

[16] T. Tran Cong and G. A. Bird. One-dimensional outgassing problem. *Phys. Fluids*, vol. 21, pp. 327–333, 1978.

[17] O. C. Zienkiewicz. *The Finite Element Method*. McGraw-Hill, London, third edition, 1977.

[18] K. W. Westerberg. *A finite element method for flow problems with free surfaces and moving fronts*. PhD thesis, University of Washington, 1992.

[19] K. W. Westerberg, C. Wiklof, and B. A. Finlayson. Time-dependent finite-element models of phase-change problems with moving heat sources. *Numer. Heat Transfer, Part B*, vol. 25, pp. 119–143, 1994.

[20] P. Hood. Frontal solution program for unsymmetric matrices. *Int. J. Numer. Methods Engn.*, vol. 10, pp. 379–399, 1976.

[21] R. S. Ransing, Y. Zheng, and R. W. Lewis. Potential applications of intelligent preprocessing in the numerical simulation of castings. In R. W. Lewis, editor, *Numerical Methods in Thermal Problems*, volume VIII, Pt. 2, pages 361–375. Pineridge Press, Swansea, 1993.

[22] R. J. Hill. *Physical Vapor Deposition.* BOC group, Inc., 1986.

[23] S. Schiller, U. Heisig, and S. Panzer. *Electron Beam Technology.* Wiley, 1982.